MDPI

Article

Representation learning of multispectral Earth Observation time series and evaluation for crop type classification

Andrea González-Ramírez [1,*], Clement Atzberger [2], Deni Torres-Roman [1] and Josué López[2]

[1] Center for Research and Advanced Studies of the National Polytechnic Institute, Telecommunications Group, Av del Bosque 1145, Zapopan 45017, Mexico
[2] Mantle Labs, Grünentorgasse 19, Vienna 1090, Austria
* Correspondence: andrea.gonzalez@cinvestav.mx

Abstract: Remote sensing (RS) spectral time series provide a substantial source of information for the regular and cost-efficient monitoring of the Earth surface. Important monitoring tasks include land use and land cover classification, change detection, forest monitoring, crop type identification, among others. To develop accurate solutions for RS-based applications, often supervised shallow/deep learning algorithms are used. However, such approaches usually require fixed-length inputs and large labeled datasets. Unfortunately, RS images acquired by optical sensors are frequently degraded by aerosol contamination, clouds and cloud shadows, producing missing observations and irregular observation patterns. To address these issues, efforts have been made to implement frameworks that generate meaningful representations from the irregularly sampled data streams and alleviate the deficiencies of the data sources and supervised algorithms. Here, we propose a conceptually and computationally simple representation learning (RL) approach based on autoencoders (AEs) to generate discriminative features for crop type classification. The proposed methodology ensembles a set of single layer AEs with very limited number of neurons, each one trained with mono-temporal spectral features of a small set of samples belonging to a class, resulting in a model capable of processing very large areas in low computational time. Importantly, the developed approach remains flexible with respect to the availability of clear temporal observations. The signal derived from the ensemble of AE is the reconstruction difference vector between input samples and their corresponding estimations, which are averaged over all cloud/shadows-free temporal observations of a pixel location. This averaged reconstruction difference vector is the base for the representations and the subsequent classification. Experimental results show that the proposed extremely light-weight architecture indeed generates separable features for competitive performances in crop type classification, as distance metrics scores achieved with the derived representations significantly outperform those obtained with the initial data. Conventional classification models were trained and tested with representations generated from a widely used Sentinel-2 multispectral multitemporal dataset, BreizhCrops. Our method achieves 77.06% overall accuracy which is $\sim$ 6% higher than using original Sentinel-2 data within conventional classifiers and even $\sim$ 4% better than complex deep models as OmnisCNN. Compared to extremely complex and time-consuming models such as transformers and Long-short term memory (LSTM), only a 3% reduction in overall accuracy was noted. Our method uses only $6.8k$ parameters, i.e., $\sim 400x$ less than OmnicsCNN and $\sim 27x$ less than Transformers. The results prove that our method is competitive in classification performance compared with state-of-the-art methods while substantially reducing the computational load.

Keywords: crop types; multispectral; multitemporal; autoencoder; representation learning

Citation: Lastname, F.; Lastname, F.; Lastname, F. Title. *Journal Not Specified* **2023**, *1*, 0. https://doi.org/

Received:
Revised:
Accepted:
Published:

1. Introduction

Spectral observations of the Earth's surface using remote sensors have been used since long time for crop type mapping, given the quantity and availability of spectral-temporal images. Multi-spectral time series from sensors such as Landsat or Sentinel-2 (S2) have

provided very cost-effective data to achieve the reliable identification and monitoring of large cropping areas [1–6]. While a wide number of data sources and supervised classification algorithms have been used for crop mapping [4,7–15], limited efforts have been made in feature learning as well as the use of un- and self-supervised learning algorithms to alleviate missing data produced by clouds. Notable overviews and examples are provided in [16–20].

The use of temporal series of multi-spectral observations for crop type classification is advantageous as the spectral differences in the crop growth, composition and structure over time are exploited [1,6,17,21]. Each crop type has a distinct seasonal spectral behavior depending on local weather and growth conditions [3,6,12]. Therefore, many researchers center their works on making use of multi-temporal information instead of using single acquisitions [1,10,22,23].

The most common methods for crop type classification are based on supervised learning algorithms [4,12,14,15,21,24–32]. The aim of these algorithms is to train a discriminative model using labeled data. However, it is often complicated to find tagged datasets for the region of interest, since it requires human intervention. Examples of supervised machine learning (ML) models include decision trees (DT) [33], extreme gradient boosting (XGBoost) [34], random forest (RF) [35], support vector machine (SVM) [36], and artificial neural networks (ANN) [37]. The mentioned algorithms provide usually similar classification performance, but often require extensive preprocessing steps such as compositing and gap-filling when incomplete (e.g., cloud-corrupted) time series are analyzed.

To mitigate the reliance on large labeled datasets, unsupervised learning aims to first derive (latent) representations from the abundant unlabeled spectral data. Representation learning (RL) is a broad subfield in machine learning, which is a set of techniques focused on automatically learning and identifying meaningful features from the input data. The derived representations encode the internal structure of the data, so that any subsequent classification needs fewer labels to be trained. In extreme cases this leads to approaches such as few-shot learning or even one-shot learning. To derive representations that efficiently encode the original data, a large number of algorithms have been developed over the past years, as for example summarized in the work of Balestriero et al. [38].

To cope with missing data in temporal observations, within the field of representation learning, different approaches have been developed as we will outline in subsection 1.1.

Autoencoders (AE) have as objective to compress data into a lower dimensional space, known as code, and then to reconstruct the input [39]. The code is regarded to be a set of features, also called representations, which condense the necessary information to recover the original data [40]. If spectral observations from a given location/pixel are tagged with the corresponding information regarding the time of observation (e.g., day of year), an autoencoder can in principle also learn to encode inputs along the time axis.

Typically, this feature of AEs is used for change detection, where the sought events are seen as anomalies in the reconstruction difference [41–43]. In technical terms, this can be framed as if the event-specific observations depart from the "normal" object-specific manifold within the embedding space. The use of ensembles of AE - each trained on different object-classes – where the resulting vectors of temporal reconstruction differences are subsequently used for classification purposes, has not been widely studied.

In this work, we propose to train a light-weight deep learning model with individual time-tagged spectral signatures, while bypassing gap-filling and compositing methods. In our framework, we use an ensemble of AEs to generate new informative and discriminative features. The features are evaluated in this work with respect to a crop type classification. Here, we arbitrarily chose one simple AE per class, but other choices would also be possible. We calculate the AEs reconstruction difference vectors between input and output and concatenate them to form a vector of representations. We evaluate the performance of the derived representations by comparing classification performance using as input data Sentinel-2 time series and the representations generated by our method on conventional classifiers, RF, SVM, XGBoost and a simple fully connected network (FCN). In addition, we

compare the outcomes against a number of more complex benchmark approaches using the same dataset.

1.1. Related work

Russwurm et al. [12] presented a satellite image time series dataset for crop type mapping named BreizhCrops. They generated top- (TOA) and bottom-of-atmosphere (BOA) time series from Sentinel-2 and used the dataset to benchmark seven classifiers for crop type mapping. A particularity of this dataset is the extremely limited number of samples for certain classes, as two minority crop types (sunflower and nuts) have much less samples than the other classes. This challenges model's capacity to effectively generalize to underrepresented classes. The difficulty to correctly classify the minority classes was even noted by the authors for high complexity benchmark models such as transformer and long-short term memory (LSTM) approaches.

Paris et al. [11] proposed an approach based on a LSTM model. They addressed the problem of cloud-corrupted multitemporal data by constructing a large training dataset from three full Sentinel-2 tiles, with orbital overlap area, to create monthly composite images. However, this approach depends on numerous cloud-clear temporal observations to generate trustworthy composites. Moreover, inaccurate cloud masks induce incorrect composite values, which compromises classification performance. The practical usage of this approach is mainly limited due to the demand for large computational resources that high complexity models require.

He et al. [18] proposed a crop type classification method, trying to improve models performance by merging spectral, textural and environmental features. One major downside of this approach is that while feature learning/selection methods attempt to reduce data redundancy, combining a large number of features easily induces redundancy, affecting classification performance. Furthermore, collecting and processing these additional features is time-consuming and computationally expensive, potentially limiting the method's scalability in larger or more diverse locations.

Lisaius et al. [44] proposed a novel representation learning approach for remote sensing data based on a twins network. They derive representations from a spectral-temporal Barlow Twin (STBT) and afterwards assess the quality of the representations within a supervised crop type classification. This method uses sparse temporal sampling as the only augmentation strategy addressing cloud-corruption issues. However, the lack of additional augmentation types restricts the model's capacity to manage other types of data corruption. As other approaches, this method assumes that cloudy observations are totally removed from the data, which is not optimum in real-world circumstances with poor quality cloud masks.

Kalinicheva et al. [43] proposed a particularly interesting approach with AEs. Reconstruction losses of joint AEs are used to detect non-trivial changes between two co-registered images in a satellite image time series. This method depends on patch-wise reconstruction error, and hence the approach has difficulty capturing fine features for objects that are only 1-2 pixels wide. Moreover, joint autoencoder models, particularly convolutional autoencoders, need significantly large training time, which makes the method unsuitable for real-time or large-scale applications.

Windrim et al. [45] proposed an approach using AEs for unsupervised feature-learning with hyperspectral data. The method allows to evaluate the separability of the feature spaces for clustering tasks. Hyperspectral data are naturally high-dimensional, and this work recognizes that high-dimensional data present issues such as greater data variability and computational complexity.

Other approaches in the state of the art address the problem of missing data with combination of optical and Synthetic Aperture Radar (SAR) data [5,24,46,47], fusion of multiple sensors [8,48,49], data interpolation [12,50] or simply using only a subset of partially cloud-free observations as Zhiwei et al [17] and Shan et al [18]. Table 1 summarizes

the related works explained before for crop types classification, highlighting the satellites used, time ranges, methods, number of classes, and feature selection techniques employed.

Table 1. Summary of relevant works related to crop types classification and representation learning.

References (year), [cites]	**Satellite**	**Time range**	**Method**	**Number of classes**	**Feature selection**
Kalinicheva, et al. (2019), [19] [43]	SPOT-5	2002 2008	AEs	Not specified	N/A
Windrim, et al. (2019), [42] [45]	AVIRIS and others	Not specified	AEs	Not specified	N/A
Paris, et al. (2020), [13] [11]	Sentinel-2	09/2017 08/2018	LSTM	12	N/A
Russwurm, et al. (2020), [65] [12]	Sentinel-2	01/01/2017 31/12/2017	ANNs	9	N/A
Zhiwei, et al. (2020), [56] [17]	Sentinel-2	23/04/2019 20/09/2019	RF	8	Spectro temporal
Shan, et al. (2022), [3] [18]	MODIS	01/01/2009 31/12/2009	KS	4	Spectral textural environmental
Leikun, et al. (2020), [35] [16]	Sentinel-2	01/04/2018 31/10/2018	RF	3	Spectro temporal
Lisaius, et al. (2024), [-] [44]	Sentinel-2	01/01/2017 31/12/2018	STBT	8	Spectro temporal
Proposal in this work	Sentinel-2	01/01/2017 31/12/2017	AEs	9	N/A

In summary, major issues in the state of the art are: 1) use of highly complex models, 2) infeasibility to scale to large areas, 3) the reliance on interpolation methods, 4) dependency on reliable cloud masks, and 5) handling of huge amount of data. Most of the machine learning-based approaches need extremely deep models leading to high computational costs and processing time, and therefore limiting scalability to process large areas of interest. Approaches that rely on interpolation methods exploit the smooth changes between data points, but fail if data gaps become overly long. Many approaches also require fixed-length sequences, which restricts the model's flexibility in dealing with irregular inputs. Sensor fusion approaches, on the other hand, face the challenge of handling huge amounts of data, which leads to high computational load and increases in processing time.

1.2. Contributions

The main contributions of this work are the following:

1. To tackle cloud-corrupted time series analysis, the proposed framework processes individual time-tagged spectral signatures for feature extraction and thereby completely avoids the use of gap-filling and compositing methods.
2. The proposed methodology uses neural networks with a reduced number of neurons to keep the computational load low, thereby facilitating the processing of large geographic areas.
3. The proposed pixel-wise framework provides a robust solution with respect to the number of available cloud-free observations, while achieving competitive results even when limited observations are available. By avoiding the use of spatial convolutions, the approach focuses on the information within the specific pixel location and thus can also be applied to regions with very small object sizes.

The remainder of this work is organized as follows. Section 2 presents the concept of RL and the respective mathematical definitions, as well as a brief description of AEs. In Section 3 the problem statement of this work and the mathematical formulation of the proposed framework are introduced. Section 4 describes quantitative and qualitative experimental results. Sections 5 and 6 present the discussion and conclusions, respectively, of the results obtained in our experiments.

2. Materials and Methods

2.1. Representation Learning

Representation learning (RL), also called feature learning, is a subfield of machine learning that aims to automatically learn and identify meaningful features, or representations, from the input data. Representations are expected to be more informative for downstream tasks such as clustering, regression, or classification, while also offering advantages in terms of model generalization and transferability [51].

In crop type classification, RL provides various benefits, especially in agricultural applications, where managing high-dimensional and complex dataset is crucial [52]. RL models first learn hierarchical features, beginning with low-level details such as edges and textures and advancing to higher-level characteristics like specific crop patterns. This hierarchy is critical for differentiating between different crop varieties [24]. Furthermore, representations derived with RL from the abundant unlabeled data mitigate the reliance on large labeled datasets, which is usually costly and time-consuming to produce in agriculture.

RL has therefore the potential to improve crop classification by automating feature extraction, enhancing generalization, reducing the need for large labeled datasets, and adjusting to environmental variability. With its scalability, speed, and capacity to combine geographical and temporal data, it is an effective tool for developing robust, accurate, and scalable crop classification models.

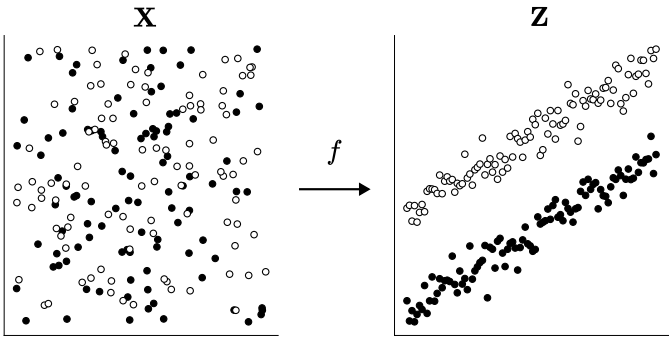

Figure 1. Illustration of representation learning (RL) as a function f, mapping vectors from a dimensional space to a representation space.

Mathematically, RL is defined as a function $f : \mathbf{X} \to \mathbf{Z}$, that transforms the input data $\mathbf{X} = \{\mathbf{x}_1, \ldots, \mathbf{x}_S\}$, into features $\mathbf{Z} = \{\mathbf{z}_1, \ldots, \mathbf{z}_S\}$, where each vector $\mathbf{x}_s \in \mathbb{R}^n$ and its image $\mathbf{z}_s \in \mathbb{R}^p$, and $\mathbb{R}^p$ denotes the representation space. The objective function f leads the model to learn meaningful representations of the input data, preserving information, reducing redundancy and generally reducing dimensionality.

In recent years, many RL methods have been proposed from different perspectives and families [38], e.g., contrastive learning methods (InfoNCE [53–55]), deep metric learning (SimCLR [56,57], NNCLR [58], etc.), non-contrastive methods (VICReg [59], BarlowTwins [44,60], etc), among others. Such approaches are particularly useful in cases where the observed data is generated by a limited set of variables [61]. However, RL is not limited to these families of methods, and conventional neural network models, such as autoenconders (AEs) can also form a representation learning method.

These approaches can also be seen as belonging to the field of self-supervised learning (SSL). Indeed, self-supervised learning techniques enable models to be pre-trained on unlabeled data, reducing reliance on labeled datasets. Furthermore, data augmentation techniques (rotations, translations, etc.) applied in these type of models have proven to improve performance without increasing the amount of training data.

2.2. Autoencoders

Autoencoders are a specific type of ANN used for unsupervised learning (Figure 2) [62,63]. They have applications in various research fields, such as anomaly detection, data compression, and feature learning. Their aim is to encode the input into a compressed representation, and then reconstruct the input from this representation, so that the reconstruction is as similar as possible to the input [51,64].

Although AEs are not in principle designed for detection and classification tasks, several works have demonstrated their potential to ease these tasks by using AE-derived data for change detection and binary classification models [41–43]. Since AEs are trained to compress and afterwards reconstruct the input data, they basically learn to model samples belonging to a certain joint distribution, leading the model to learn class-specific properties.

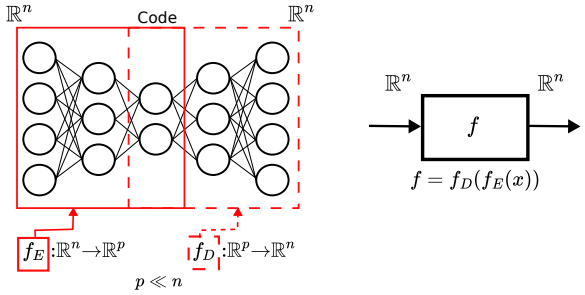

Figure 2. Example of an autoencoder architecture with mathematical definition as a function. In the present work, the reconstruction difference between input and output is used as representation, and not the code itself.

The aim of the AEs, formally defined in [65], is to learn the functions $f_E : \mathbb{R}^n \to \mathbb{R}^p$ and $f_D : \mathbb{R}^p \to \mathbb{R}^n$, where f_E denotes the encoder function, f_D is the decoder function, n is the dimension of the input and output spaces, and p denotes the dimension of the code space. Generally $p \ll n$, leading to learn compressed features of the data.

3. Proposed method

Consider an annual multi-spectral time series dataset acquired by an optical sensor, i.e., each sample has been acquired at different times. From the entire set of observations, only a subset will usually be useful as weather conditions such as clouds, cirrus, cloud shadows, snow, among others, occasionally obstruct the land surface. Missing data produced by these conditions commonly leads to poor performance on particular tasks, such as land use / land cover classification or change detection. Therefore, it is of utmost importance to extract and use only the land related information, either by filtering the data, or generating new features (often in the form of composites).

3.1. Problem statement

Let $\mathscr{X} \in \mathbb{R}^{P\times B\times T}$ be a multispectral time series dataset represented as a third-order array, where P represents the number of geographic points on the earth surface, B is the number of spectral bands, and T denotes the number of temporal observations, and each geographic point is denoted as a vector $\mathbf{x} \in \mathbb{R}^{B\cdot T}$ and $\mathbf{x} \in \mathscr{X}$. The aim is to transform each vector $\mathbf{x}$ into a representation vector $\mathbf{z} \in \mathbb{R}^R$, where R is the number of new features named representations. The representation vector $\mathbf{z}$ addresses label scarcity and missing data produced by clouds, and permits downstream tasks such as crop type classification (See Figure 3).

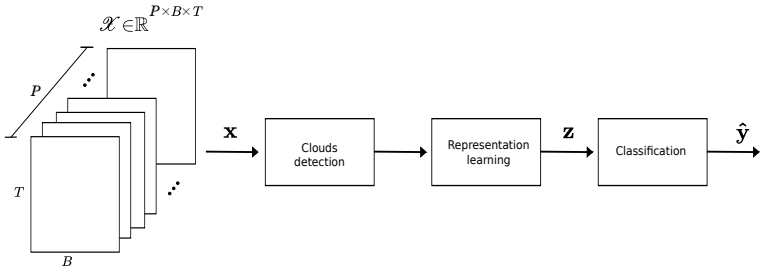

Figure 3. First level of the proposed workflow. Scene classification product provided by the European Space Agency (ESA) is used to mask out cloudy samples from a geographic point (pixel) shaped as a $T \times B$ array.

3.2. Methodology

The methodology of this work consists of four processes: data downloading and preprocessing, model training, inference (representations formation) and, as downstream task to evaluate the quality of the derived representations, classification. The proposed framework is shown in more detail in Figure 4.

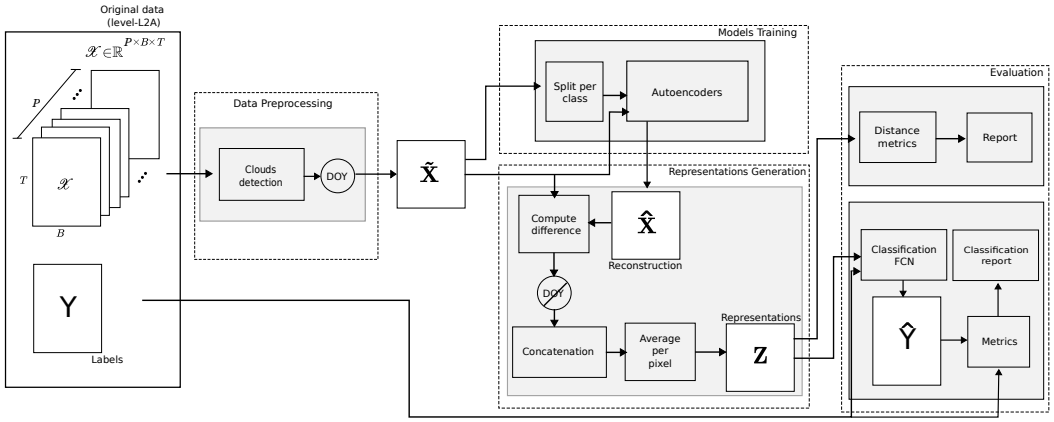

Figure 4. Proposed framework block diagram. The full methodology is composed by four main blocks: data preprocessing, model training, representation generation and evaluation.

3.2.1. Data downloading/preprocessing

Reference crop type labels were extracted from a public benchmark dataset named BreizhCrops [12] (field level). Google earth engine (GEE) was used to download full multi-temporal multispectral data from a region of interest (ROI) (see Figure 5).

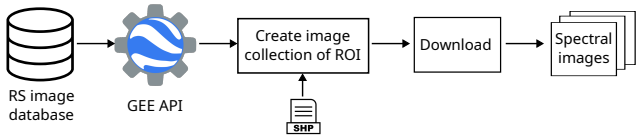

Figure 5. Dataset downloading process using the google earth engine (GEE) database.

Given the multispectral time series, a scene classification product (e.g., ESAs sen2cor) is used to get a cloud/non-cloud mask for each sample $\mathbf{x}$, i.e., for each temporal observation at pixel level. Cloudy samples are excluded from the dataset. This creates a set of pixels with variable number of cloud-free (temporal) observations. Only the cloud-free observations of a pixel are the inputs to generate a representations vector. This makes our model flexible and independent on the number of clear observations.

To leverage the temporal information for the particular task of crop type classification, we add temporal embeddings to each sample, with the aim to extend the vector space to one where similar spectral curves of different crop types at different growth stages are

separable. We use the sine and cosine functions to model the annual periodic phenomenon presented by the cyclical character of the nature seasons and crops evolution between planting and harvest. As day 1 and 365 are in principle distant but with similar natural conditions, we embed time by scaling the acquisition day-of-year (DOY) to (0, 1) range dividing by 365 and then place them on a real value scale by computing the sine and cosine. This makes each scaled DOY a unit vector decomposed into two orthogonal vectors, regarded as spring–fall axis (sine), and summer–winter axis (cosine) giving to our method the capacity to perform correctly in different earth latitudes [66].

Hence, each sample $\tilde{\mathbf{x}} \in \mathbb{R}^F$ has F features, i.e., B spectral bands plus two values denoting the sensing DOY, computed as follows

$$doy_{\sin} = \left(\sin\left(\frac{2\pi doy}{365}\right) + 1\right)/2 \tag{1}$$

and

$$doy_{\cos} = \left(\cos\left(\frac{2\pi doy}{365}\right) + 1\right)/2, \tag{2}$$

where doy denotes the DOY as a numeric value from 1 to 365, and $doy_{\sin}$ and $doy_{\cos}$ are in the range 0 to 1.

3.2.2. Model training

The principle of this work is to train a set of C independent AEs with vectors $\tilde{\mathbf{x}}_c$, which are individual time-tagged spectral signatures of cloud/shadows-free observations that belong to a particular class c for $c = 1, \ldots, C$, resulting in C semi-supervised trained models able to reconstruct samples from the same class, approaching the reconstruction difference to the zero vector, while using the ensemble of reconstruction difference vectors to derive the representations (see Figure 6).

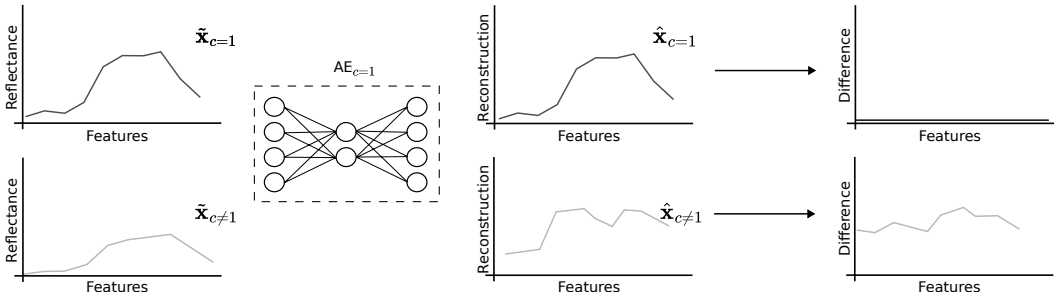

Figure 6. Example of the expected output for positive and negative samples. The difference from the ensemble of autoencoders (AEs) constitute the representations for the downstream task.

The training process of the AEs can be semi-supervised, given a labeled dataset, as in this work, or unsupervised, with no ground truth data (e.g., by training a set of random AEs not associated to specific crop types or classes). The scope of this work addresses the semi-supervised approach, with a crop type labeled dataset as pairs (x, y), where y is an integer value which indicates the class that x belongs to. Samples are split in as many subdatasets as classes and each subdataset is used to train a different AE. This process is graphically represented in Figure 4 as model training and further illustrated in Figure 7.

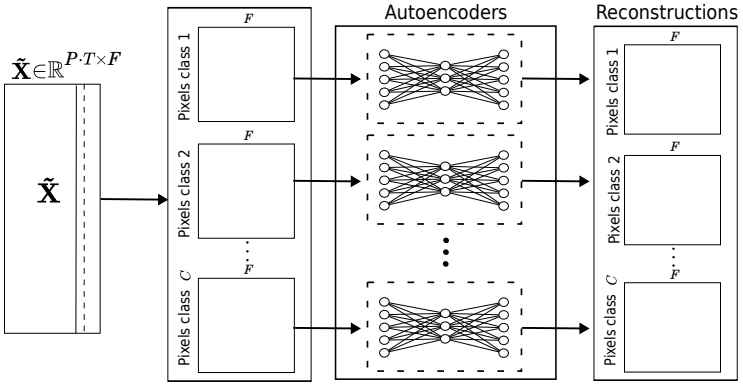

Figure 7. Autoencoders (AEs) training. Each autoencoder is trained with a finite set of individual spectral curves belonging to one of the crop types. The reconstructions from the C classes are used to calculate the difference vector across the ensemble, that is the final set of representations.

As mentioned in Section 2.2, an AE is formally defined as a composite function $f_{AE}(\mathbf{x}) = f_D(f_E(\mathbf{x}))$. For our input vectors $\tilde{\mathbf{x}}$, each AE can be seen as a function

$$f_{AE}(\tilde{\mathbf{x}}) = f_D(f_E(\tilde{\mathbf{x}}))) = \hat{\mathbf{x}} \tag{3}$$

where, $f_E(\tilde{\mathbf{x}})$ denotes the encoder function, which maps the input vectors, from the input space $\mathbb{R}^F$ to an embedding space $\mathbb{R}^P$, known as code, and $f_D(\cdot)$ maps the code to an estimated reconstruction $\hat{\mathbf{x}}$ of the input vector. Since our architecture has C AEs, then it has C composite functions $f_{AE}^{(c)}$, for $c = 1, 2, \ldots, C$. Each AE is trained with a set of vectors belonging to a single class, and consequently a particular $f_{AE}^{(c)}$ is learned. In general,

$$\hat{\mathbf{x}}_c^{(c)} = f_{AE}^{(c)}(\tilde{\mathbf{x}}_c) \tag{4}$$

where $\tilde{\mathbf{x}}_c$ denotes the input vector belonging to class c, $f_{AE}^{(c)}$ is the AE function associated to the c-th class, and $\hat{\mathbf{x}}_c^{(c)}$ is the output vector delivered by the c-th AE.

3.2.3. Representations generation (Inference)

Given the C trained AEs, denoted as $f_{AE}^{(c)}$, the set of cloud-free observations of individual geographic points (pixels) forms an array $\tilde{\mathbf{X}} \in \mathbb{R}^{t \times F}$, where t denotes the number of cloud-free samples for a given pixel. $\tilde{\mathbf{X}}$ is the input to the AEs functions, and the reconstruction array is obtained from each AE as

$$\hat{\mathbf{X}}^{(c)} = f_{AE}^{(c)}(\tilde{\mathbf{X}}) \tag{5}$$

where $\hat{\mathbf{X}}^{(c)}$ represents the reconstruction estimated by the c-th AE.

Then, the t difference vectors associated to a single pixel which form an array $\mathbf{D}^{(c)}$ are computed by

$$\mathbf{D}^{(c)} = \left| \tilde{\mathbf{X}} - \hat{\mathbf{X}}^{(c)} \right|^{\text{abs}} \tag{6}$$

where $d_{ij}^{(c)} = \text{abs}(\tilde{x}_{ij} - \hat{x}_{ij}^{(c)})$. Let $\mathbf{d}_i^{(c)}$ be the rows of $\mathbf{D}^{(c)}$, then the pixel mean reconstruction difference vector $\bar{\mathbf{d}}^{(c)} \in \mathbb{R}^F$ is computed by

$$\bar{\mathbf{d}}^{(c)} = \frac{1}{t} \sum_{i=1}^{t} \mathbf{d}_i^{(c)} \tag{7}$$

and the representation $\mathbf{z}$ of the pixel $\tilde{\mathbf{X}}$ is formed by the concatenation of the C vectors $\bar{\mathbf{d}}^{(c)}$ as

$$\mathbf{z} = \bar{\mathbf{d}}^{(1)} \oplus \bar{\mathbf{d}}^{(2)} \oplus \cdots \oplus \bar{\mathbf{d}}^{(C)} \tag{8}$$

where $\oplus$ denotes the vector concatenation and $\mathbf{z} \in \mathbb{R}^R$. The inference phase of our proposed framework is presented in Figure 8.

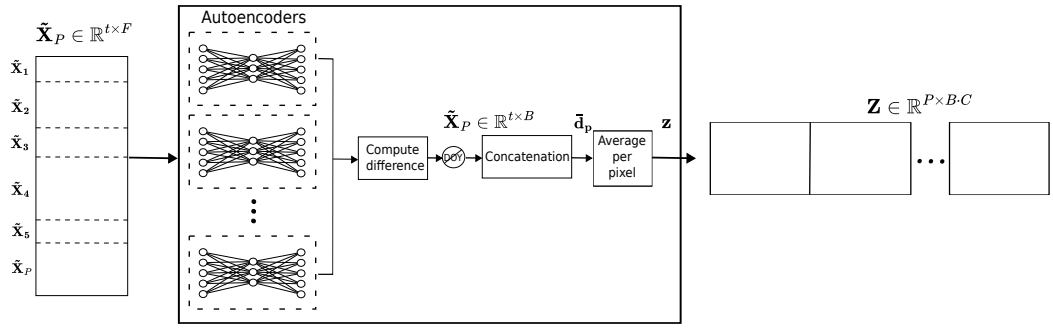

Figure 8. Inference workflow of the proposed framework. For each temporal set of cloud-free reflectance spectra, the average reconstruction difference vector are calculated for each of the C autoencoders (AEs) and concatenated to define the representations of this pixel.

4. Experimental results

4.1. Dataset

The public benchmark dataset *Breizhcrops* presented in [12] was used for experiments and evaluation. This dataset is available at the GitHub repository (https://github.com/dl4sits/breizhcrops). The provided multi-temporal multi-spectra data is from the Brittany region in the northwest of France and is composed of labeled Sentinel-2 images from January 1st to December 31st, 2017. Labels are assigned to the "average of reflectance values over the bounds of the field geometry retrieved from the dataset" [12].

This dataset is organized in four regions (see Table 2), and each region contains nine crop categories: barley, wheat, rapeseed, corn, sunflower, orchards, nuts, permanent meadows and temporary meadows. In [12], regions FRH01 and FRH02 were used for training, FRH03 for validation, and FRH04 for evaluation.

Table 2. Regions of Brittany (France) with number of field parcels and spectral data for the atmospherically corrected surface reflectances at the bottom-of-atmosphere (L2A) [12]. The regions FRH01 and FRH02 were used for training, FRH03 for validation, and FRH04 for evaluation.

Regions	NUTS-3	L2A
Côtes-d'Armor	FRH01	178,632
Finistère	FRH02	140,782
Ille-et-Vilaine	FRH03	166,367
Morbihan	FRH04	122,708
Total		608,489

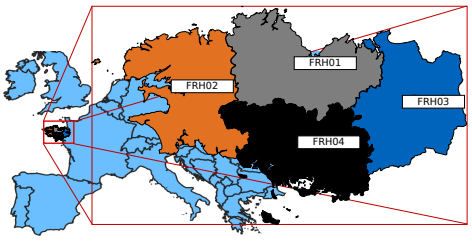

Table 3 describes the number of samples per class used for training, validation and test respectively. It is worth noting that the dataset is highly imbalanced; the most abundant class "temporary meadows has $>$ 300 times samples compared to the two minor classes "sunflower" and "nuts". This makes the classification model more sensitive to overfitting and also makes an accuracy evaluation more difficult [67]. To ensure perfect comparability with previously published work [12] we have chosen to keep the dataset without any modifications.

Table 3. Number of samples per class used for training, validation and test.

Class	Training	Validation	Test	Total
Barley	23,787	7,154	5,981	36,922
Wheat	45,406	27,202	17,009	89,617
Rapeseed	7,945	3,557	3,244	14,746
Corn	80,623	42,011	31,361	153,995
Sunflower	7	10	2	19
Orchards	1,285	1,217	552	3,054
Nuts	28	10	11	49
Perm. Meadows	69,177	32,524	25,134	126,835
Temp. Meadows	91,156	52,682	38,414	182,252

It is worth mentioning that this dataset provides only spectral signatures in tabular format for the center pixel in a field and not Sentinel-2 images.

4.2. AEs training

With the aim of developing an algorithm capable to process relatively large geographic areas, the AEs are composed by a single-layer FCN as encoder, and its counterpart for the decoder. While other models, such as convolutional and recurrent networks, require a relatively large number of trainable parameters, as described in [4,11,12], the single layer AEs that form our model need considerably fewer units, meaning lower computational load and faster processing times.

The batch size, learning rate, number of units in the hidden layer, and loss function were set in accordance with the results acquired through the hyperparameter random search presented in Appendix A. The split of the dataset is described in Table 4, which outlines the features employed in this experiment. These include DOY (sine and cosine), 10 spectral bands (10 and 20 meters resampled to 10m) and five well-known spectral indices: Normalized difference water index (NDWI), Normalized difference vegetation index (NDVI), Normalized difference tillage index (NDTI), Normalized difference of senescent vegetation index (NDSVI) and Enhanced vegetation index (EVI). Table 5 presents the AEs configuration.

Table 4. Training, validation and testing split, and number of input features and classes considered for the autoencoders.

Parameter	Value
Training size	319,414
Validation size	166,367
Testing size	122,708
Features	10 bands, 2 DOY, 5 spectral indices
Classes	9

Table 5. Autoencoders (AEs) hyperparameters final configuration established by random search.

Hyperparameter	Value
Epochs	10000
Early stop	True
Patience	10
Min. delta	1e-5
Batch size rate	0.05*
Units in hidden layers	5
Learning rate	1e-4
Optimizer	Adam
Loss	MSE

* proportion of samples for each class

4.3. Separability assessment and distance metrics

For qualitative assessment of the inter-class separability in the generated representation space, 3D scatterplots of the test spectral-temporal Sentinel-2 BOA data and their corresponding representations produced by our method, reduced to a three-dimensional space by t-distributed Stochastic Neighbor Embedding (TSNE), are shown in Figures 9a and 9b respectively. The figures show that the density of points belonging to each of the crop types is much better clustered.

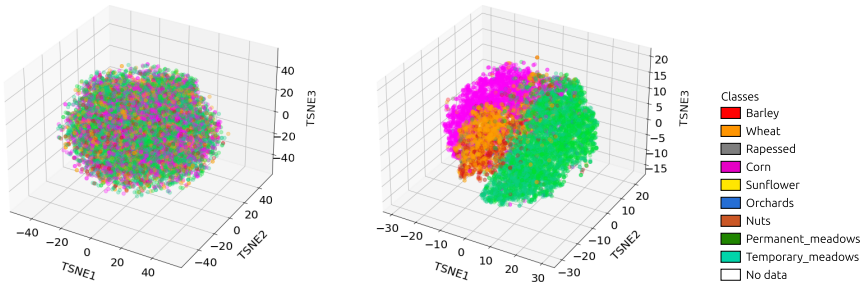

(a) **(b)**

Figure 9. 3D-scatterplot of (a) S2 fixed-length time series (45 observations) and (b) representation, over three principal components obtained by t-distributed Stochastic Neighbor Embedding (TSNE) only for visual interpretation.

Several distance metrics were used to quantify the distance between classes. Table 6 presents a comparison of the inter-class separability on the input spectral-temporal Sentinel-2 BOA data and the generated representations, measured by: Silhouette score (SS), which ranges from -1 for incorrect clustering and +1 for highly dense clustering, Calinski-Harabasz index (CH), for which larger scores indicates better separability, and Davies-Bouldin index (DBI), which ranges from 0 to ∞ and the closer to zero the better the separability between clusters (see Appendix B for metrics definitions).

The distance scores again demonstrate much higher separability in the representation space than on the initial data.

Table 6. Class distance assessment of the S2 dataset and the representations produced by our method. Silhouette score (SS), Calinski-Harabasz index (CH), Davies-Bouldin index (DBI).

Distance metric	S2 data	Our approach
SS	-0.76	**0.20**
CH	1.4	**73074.46**
DBI	72.44	**18.96**

4.4. Evaluating representations in the classification of crop types

Once the representations have been produced, a 3-layer FCN was used as classification model, where the inputs are the generated representations and their corresponding labels. The parameters of the classifier are detailed in Table 7. Note that the input dimensionality is defined by B spectral bands plus 5 spectral indices times C number of AEs, as the DOY embeddings would induce redundancy.

Table 7. Classification model configuration.

Hyperparameter	Value
Input size	$(B+5) \times C = 135$
Epochs	10000
Batch size	1000
Units in hidden layers	128, 64, 32
Learning rate	1e-4
Optimizer	Adam
Loss	Categorical crossentropy

A comparative study is presented in Table 8 where the performance of different traditional classifiers, such as RF, SVM, XGBoost, and FCN, are evaluated using two types of input data: fixed length Sentinel-2 BOA data and our derived representations. The evaluation is based on overall accuracy (OA), Cohen's kappa coefficient (κ) and Matthews correlation coefficient (MCC). All models are tested with exactly the same training and

testing samples of the BreizhCrops dataset (as described in Table 3) allowing a direct comparison of results.

In all cases, our representations improved classification performance compared to the use of the original Sentinel-2 data. Improvement ranged from $\sim$ 2% to $\sim$ 7% in terms of OA. The FCN classifier achieves the best OA, κ and MCC with both input types, and stands out particularly using the representations as input, reaching the highest OA=0.7706, κ=0.6995 and MCC=0.7014.

Table 8. Comparison of classification performance with Sentinel-2 data versus representations produced by our method as input data to conventional classifiers, random forest (RF), support vector machine (SVM), extreme gradient boosting (XGBoost) and fully connected network (FCN) evaluated by overall accuracy (OA), Cohen's kappa coefficient (κ), and Matthews correlation coefficient (MCC).

	S2 data				Representations			
Metric	RF	SVM	XGBoost	FCN	RF	SVM	XGBoost	FCN
OA	0.7172	0.7091	0.7036	0.7438	0.7345	0.7466	0.7139	**0.7706**
κ	0.6264	0.6197	0.6113	0.6716	0.6464	0.6688	0.6201	**0.6995**
MCC	0.6326	0.6249	0.6149	0.6729	0.6491	0.6710	0.6234	**0.7014**

We conducted a comparison between representations and S2 data across all classifiers in scenarios with limited labeled data. Results presented in Figure 10 demonstrate that the representations consistently offer greater stability and maintain higher accuracy as the percentage of available training data decreases.

The FCN benefits exceptionally from representations, it obtains the highest OA of $\sim$ 0.77 using 100% of the training data, and its classification performance is much less affected compared to the use of the original Sentinel-2 data as the number of training samples decreases. SVM, in combination with the representations, keeps the classification performance stable, even with very low number of training samples (around 30,000), offering clear improvements over S2 data and making it the best option in this scenario. XGBoost and RF, on the other hand, offer stable performance with S2, but the use of representations considerably elevates accuracy.

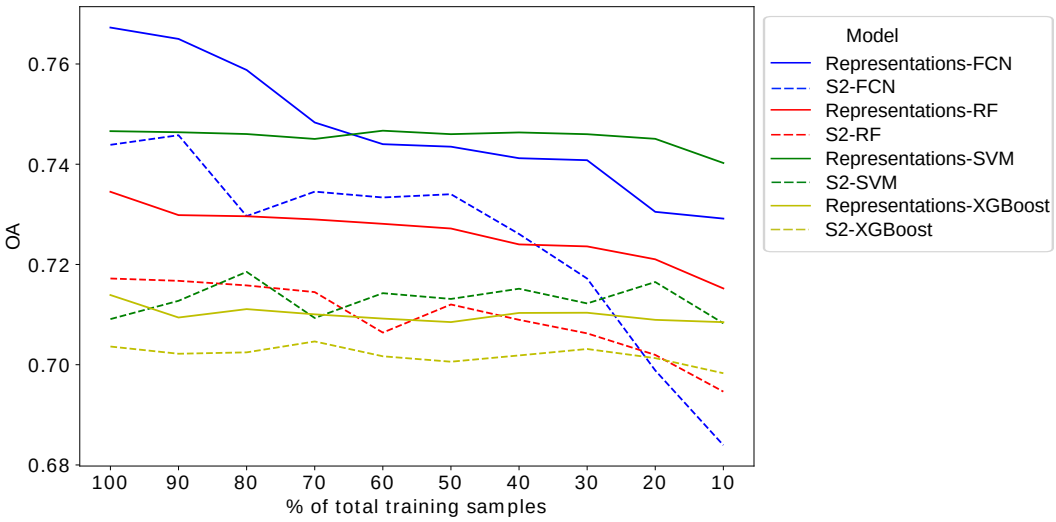

Figure 10. Overall Accuracy (OA) of random forest (RF), support vector machine (SVM), extreme gradient boosting (XGBoost) and fully connected network (FCN) trained with variable percentage of training samples and using (i) representations (solid line), and (ii) original Sentinel-2 data (broken line).

The confusion matrix shown in Table 9 presents the model performance on the testing dataset. Our approach performs relatively accurate for wheat, rapeseed and corn samples, and, although permanent and temporary meadows samples are not accurately classified,

both classes are actually the same crop type, and misclassified samples are mainly due to their similar nature as shown in the last two rows of the confusion matrix. However, our approach is inaccurate for the small classes in this dataset, i.e., sunflower and nuts, which can not be separated due to the very limited samples provided. The misclassification of these classes is probably not related to incapacity of the model to deal with imbalanced datasets, but is a direct result of the very limited number of samples, as was also outlined by the authors in [12]. As the spectral signatures provided in the dataset are field-based averages, classes such as orchards, where trees only cover single pixels with large areas between the trees, are easily confused by our model with regular parcels of meadows.

Table 9. Confusion matrix of the fully connected network (FCN) prediction for the testing data.

Object based	Barley	Wheat	Rapeseed	Corn	Sunflower	Orchards	Nuts	Permanent meadows	Temporary meadows
Barley	4608	642	71	231	0	0	0	29	400
Wheat	626	15681	14	206	0	0	0	79	406
Rapeseed	130	17	2949	31	0	0	0	15	102
Corn	236	314	38	29900	0	0	0	111	762
Sunflower	0	0	0	0	0	0	0	1	1
Orchards	0	5	1	4	0	0	0	277	265
Nuts	0	0	0	2	0	0	0	6	3
Permanent meadows	122	212	4	163	0	0	0	12409	13224
Temporary meadows	451	321	64	628	0	0	0	7942	29008

Table 10 presents a performance comparison of our method with much deeper models, such as convolutional, recurrence and attention-based methods. TempCNN, OmniscCNN, LSTM, StarRNN, Transformer presented in [12] and our proposed method are evaluated by OA, average precision (AP), F1 score, and κ. Additionally, the number of parameters and runtime in iterations per second (it/s) are presented. We present the results reported in [12]. Notwithstanding, the same test data points were used in our experiments, hence, results are directly comparable.

Table 10. Classification performance evaluation of benchmarked models by overall accuracy (OA), average precision (AP), F1 score (F1) and Cohen's kappa coefficient (κ). All models were evaluated over the same testing dataset and on a processor Intel® Core™ i5-7200U CPU @ 2.5GHz, 4 cores, Dell Inc. Inspiron 15-3567 Intel® HD Graphics 620 (KBL GT2). In bold the best results are highlighted.

	TempCNN	OmniscCNN	LSTM	StarRNN	Transformer	**AE-FCN**
OA	0.79	0.73	**0.80**	0.79	**0.80**	0.77
AP	0.55	0.52	0.57	0.56	0.58	0.54
F1	0.79	0.72	0.80	0.79	0.80	0.76
κ	0.73	0.65	0.74	0.73	0.75	0.70
N° param	3,199,501	2,739,737	1,339,431	72,103	188,429	**6,825**
Runtime in $[it/s]$	0.70	0.07	0.12	0.22	0.44	**23.8**

Our representations-based approach combined with the FCN is substantially less computationally expensive than the other benchmarked methods, requiring only 6,825 trainable parameters, compared to the 1,338,431 for LSTM and 188,429 for Transformer. This means that our method uses roughly 200 and 28 times fewer parameters, respectively, compared to the two deep learning methods. This reduction directly impacts computational load and consequently processing time, as seen in the runtime of 23.8 it/s obtained with our method, which is more than 30 times higher than the best of these deep models in terms of runtime, TempCNN (0.70 it/s) and more than 50 times higher than Transformer (0.44 it/s).

In addition to this substantial reduction of trainable parameters, our method maintains competitive classification accuracy, achieving an OA of 0.7706, just 3% lower than Transformer's OA of 0.80. Furthermore, the accuracy of our method is comparable to TempCNN (OA=0.79) and 4% better than OmniscCNN (OA=0.73). However, these two approaches are

computationally far more expensive, requiring approximately 400 times more parameters than AE-derived representations within a simple FCN (AE-FCN).

In terms of metrics that weight class imbalance, LSTM and Transformer obtained the highest F1 score (both 0.80), whereas AE-FCN achieves a competitive 0.76, indicating a balanced performance despite having far fewer parameters. Similarly, LSTM and Transformer have the highest κ score (0.75), with AE-FCN scoring 0.70, which is penalized owing to mismatches in particular classes but remains effective given the model's simplicity.

4.5. Qualitative results

To enable a qualitative analysis over a contiguous spatial extent and not simply on a tabulated dataset, 67 Sentinel-2 multispectral images from 2017 of a subregion in FRH04 (test region) were downloaded and preprocessed. A representative area was defined drawing a polygon where most of the classes (barley, wheat, corn, rapeseed, temporary meadows and permanent meadows) are present (Figure 11a).

Representations for this study area are produced by passing individual pixels from the imagery dataset through the inference workflow outlined in Figure 8. Composite images generated by combining three random representations are presented in Figures 11b, 11c, 11d, 11e, 11f, 11g and 11h, which clearly contrast the crop fields in the new representation space.

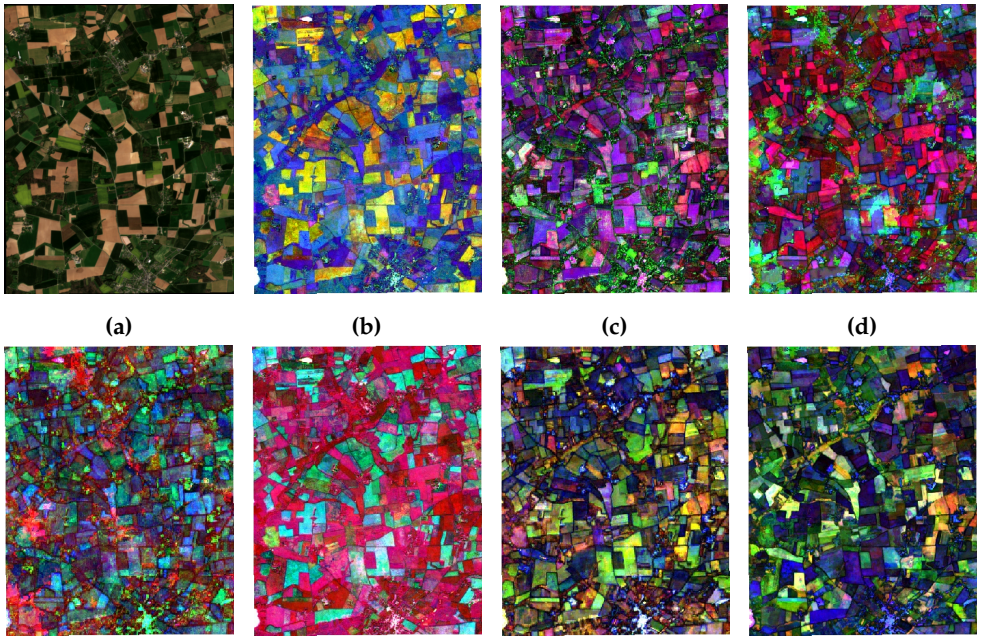

Figure 11. (a) True color image of the study area in 2017 and composites images generated by combining three random representations per map (b) 9-64-30, (c) 59-84-81, (d) 30-11-141, (e) 45-66-57, (f) 20-10-32, (g) 5-142-83 and (h) 24-79-133.

A classification map produced by our method is presented in Figure 12. Figure 12b illustrates a pixel-based classification, i.e., without considering field boundaries or spatial context. Misclassifications are mainly seen near field edges, since these are not pure pixels and often contain mixed spectral data.

To better illustrate the potential of our method in real-world activities, Figure 12c presents a field-based classification map, where the output of our method is post-processed to group the pixel-wise predictions into polygon-level prediction by computing the mode of predictions within the field borders. This map preserves field structure, creating a more coherent and interpretable map. The strong similarity between Figures 12a and 12c show

that the representations are sufficiently representative for crop type classification. Figure 12d is a map showing correctly classified fields in green and misclassified fields in red.

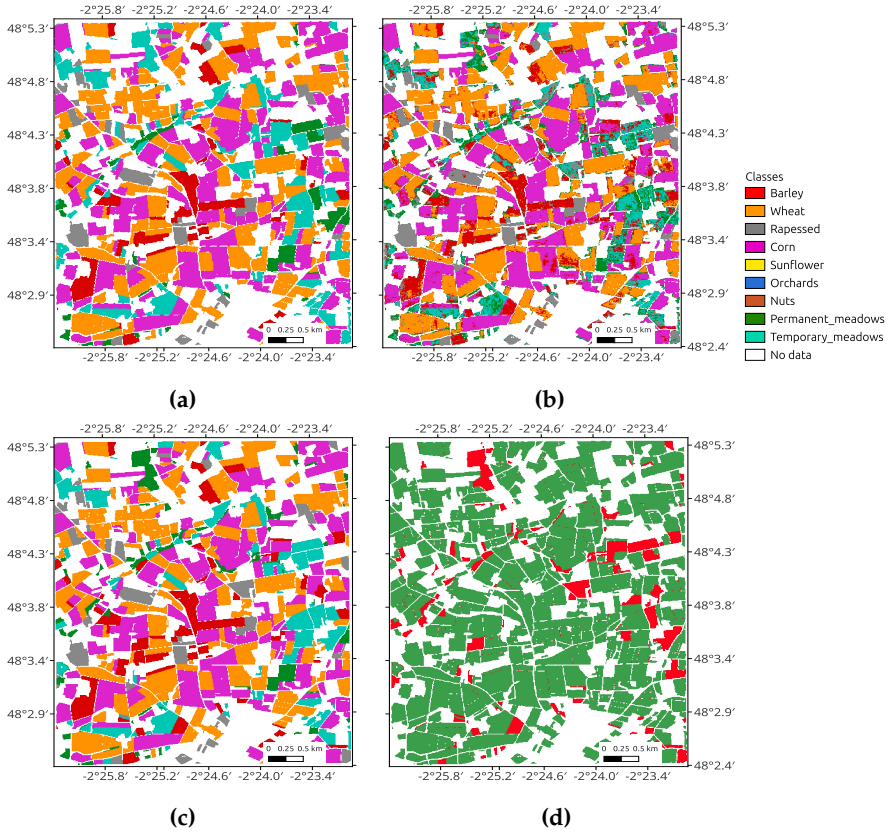

Figure 12. (a) Study area ground truth at field level (polygons), (b) representations-based fully connected network (FCN) pixel-wise classification (raster), (c) representations-based FCN field-based classification (polygons) and (d) map of correctly classified fields in green and misclassified fields in red.

As reported in the confusion matrix (Table 9), qualitative results illustrate that temporary meadow fields are frequently confused with permanent meadows. However, as discussed in subsection 4.4, these two crop type share similar spectral signatures, particularly when observed during different seasons of the year. This spectral overlap makes it challenging for classifiers to distinguish between these two crop types.

5. Discussion

Our AEs-based methodology for RL addresses the problem of cloud-corrupted optical data by mapping RS spectral-temporal features into informative, and gap free representations. Our spectral and temporal-based approach produces pixel level comprehensive representations, while avoiding the need to employ complex spatial-based classifiers.

The method proposed in this paper has as main advantage its ability to produce pixel-wise representations independently of the number of cloud-free samples, as any number of valid observations (e.g., cloud-free observations per pixel or object) can be handled seamlessly, and we can implement our method as a in-season approach without any further modifications, as the concatenation of (residual) vectors from the AEs builds on the average reconstruction difference which can be computed whenever desired in a given growing season.

The focus of our work is on the use of EO time series without common pre-processing steps such as complex interpolation, gap filling, compositing or hand-crafted feature extraction methods, used in other approaches. The derived representations from our method will be gap free as long as at least one valid observation is present in the time series,

but the stability of the representations would in principle increase when larger number of valid observations are available (See Section 3.2.2 and 3.2.3).

Despite the restricted depth of our method for, both (i) the representations learning process, as well as for (ii) the classifier, our method performs satisfactorily. While some deep classification networks achieve slightly better OA scores, our lightweight model performs similarly with substantially less computational load, as can be seen in Table 10. The use of the derived representations instead of directly using the Sentinel-2 spectral-temporal data improves performance on all baseline models presented in Table 8, while maintaining low computational load. The usefulness of the representation increased compared to the original data when fewer training samples are available for training. In this work we show that despite the computational simplicity of our framework/model, we achieve good classification results also compared to computationally much more complex approaches.

Models, such as TempCNN, OmniscCNN, LSTM, StarRNN, and Transformer, presented in Table 10, need to be executed on powerful equipment well-suited for handling complex models to achieve low processing times. In contrast, our full framework is easily launched on a significantly powerless CPU. This showcases our method's efficiency and adaptability to lower-end hardware and/or to process large geographic areas requiring much less computational resources. In terms of number of trainable parameters, convolutional and recurrent models require millions of parameters, which indicates their high computational demands, while our method only requires thousands of parameters.

The dataset used in the experiments of this work is particularly challenging, as sunflower and nuts were not separable by any of the presented algorithms, mainly due to the limited number of labeled samples. The few available samples restricts all of the models presented in Tables 8 and 10 from learning enough informative and significative representations before classification.

Although our method fully integrates phenological information, by learning a representation, representing the entire time series acquired within one year/season, the accuracy saturates at some point when varying the number of training samples (Figure 10), simply because not all classes can be separated by the data at hand, as is the case for permanent and temporary meadows. Here other sensor systems should be integrated (e.g. microwaves, thermal, multi-angle instruments, etc.).

As other methods, our approach is still negatively affected in classification performance when extraordinarily limited number of samples are available. A simple solution is to expand labeled data collection, even using samples from other already labeled regions and with similar phenological conditions. In addition, our approach can be easily adapted to process different areas and even with other optical sensors datasets, such as Landsat or radar sensors. However, we are convinced that a better solution would be a model able to perform accurately with minimum amounts of sample data. For this reason, efforts on representation learning based methods would help to generate condensed spectral temporal features which generalize better, and are stable over years. Work is underway to see how classification performance changes if the AEs are trained without focusing on specific classes. If successful, this would yield a fully self-supervised learning algorithm for representation learning.

6. Conclusions

Based on the results reported in this paper, we draw the following conclusions:

1. The quantitative evaluation based on various distance metrics demonstrates that the representations produced by our method accomplished the objective of mapping RS spectral-temporal raw data (e.g., Sentinel-2) to a feature space where inter-class separability is higher than in the initial Sentinel-2 BOA time series.
2. The classification scores achieved by our method, alongside the comparison of trainable parameters and execution time, highlight the efficiency of our method. Our model outperforms conventional classifiers in terms of accuracy, all with significantly

reduced computational load. This allows large areas to be processed without excessive time consumption, offering an effective balance between performance and efficiency.
3. Our method performs well for the majority of classes evaluated in this work, especially for those with sufficient training samples. When only few training samples were available, our method showed the same problems as the baseline methods.

In summary, experimental results demonstrate that this work successfully introduce a novel RL method for crop type classification and confirm the main characteristics of our method: 1) ability to process large areas of interest, as it is often required in real-world activities, 2) input length flexibility and no reliance on gap filling methods, 3) competitive trade-off between computational demands and classification performance, and 4) direct applicability for other downstream tasks.

Outside the scope of this work, there are still some points to consider in future research:

- Implementation of a fully unsupervised methodology for training autoencoders without relying on labeled data.
- Evaluation of the proposed methodology on other optical sensors, radar sensors or combination of several sensor modalities.
- Fine-tuning the RL-classification model to find a better balance between performance metrics and number of trainable parameters.
- Although this research presents specifically crop type classification task-guided representations, the extrapolation to other classification task is straightforward.
- Study of the impact of high cloud cover conditions by artificially removing cloud-free (valid) observations on classification accuracy. While our framework can handle time series with missing data, the robustness of the method in low-quality time series is not specifically addressed in this paper.

Author Contributions: Conceptualization, A.G. and C.A.; methodology, C.A., A.G. and J.L.; software, A.G. and J.L.; writing—original draft preparation, A.G. and J.L.; writing—review and editing, C.A. and D.T.; visualization, A.G.; supervision, C.A. and D.T.; project administration, A.G.; funding acquisition, D.T., C.A., J.L., A.G.

Funding: This research was funded by CONAHCYT grant number 1001207.

Conflicts of Interest: The authors declare no conflict of interest

Abbreviations

The following abbreviations are used in this manuscript:

AEs	Autoencoders
ANN	Artificial neural networks
AP	Average precision
BOA	Bottom of atmosphere
CH	Calinski harabasz
DBI	Davies bouldin index
DOY	Day-of-year
DT	Decision trees
FCN	Fully connected network
GEE	Google earth engine
κ	Cohen's kappa coefficient
KS	Kennard–Stone
LSTM	Long-short term memory
MCC	Matthews correlation coefficient
ML	Machine learning
MSE	Mean square error
OA	Overall accuracy
PCA	Principal component analysis
RF	Random forest
RL	Representation learning
ROI	Region of interest
RS	Remote sensing
SS	Silhouette score
STBT	Spectral-temporal Barlow twins
SVM	Support vector machine
TOA	Top of atmosphere
UA	User's accuracy
XGBoost	Extreme gradient boosting

Appendix A Hyperparameters random search

AEs hyperparameters were defined after an extensive random search. One hundred configurations with four variable hyperparameters were launched and evaluated with three classification and three distance metrics. The search spaces for each hyperparameter are:

- Units: $U\{1, 16\}$
- Batch size rate: $U[0.1, 0.3]$
- Learning rate: $U\left[1 \times 10^{-3}, 9 \times 10^{-6}\right]$
- Loss: $\{0, 1\}$

where $U\{\cdot\}$ and $U[\cdot]$ denote uniform discrete and continuous distribution respectively. Final configuration reported in Table 5 was defined according to the pairwise correlation between hyperparameters and metrics presented in Figure A1.

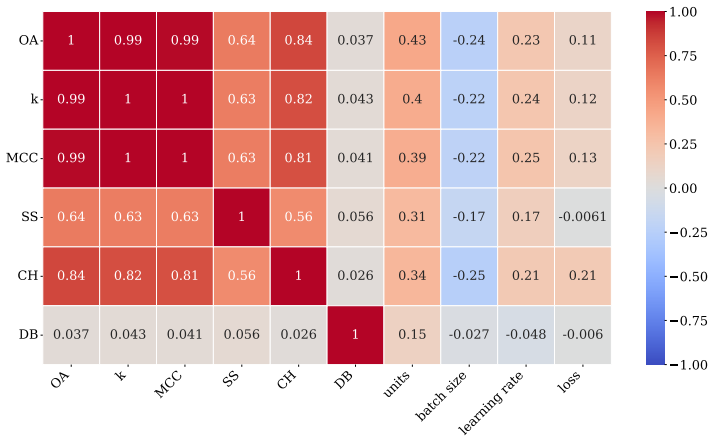

Figure A1. Hyperparameters and quality indicators correlation matrix.

Appendix B Separability metrics

These metrics quantify how separable a set of classes/clusters are from each other.
Silhouette score:

$$SS = \frac{b - a}{max(a, b)} \tag{A1}$$

where a is the mean distance between a sample and all other points in the same class, b is the mean distance between a sample and all other points in the next nearest cluster. The score is bounded between -1 for incorrect clustering and +1 for highly dense clustering.

Calinski-Harabasz Index

$$CH = \frac{\left[\frac{\sum_{k=1}^{K} n_k \|c_k - c\|^2}{K-1}\right]}{\left[\frac{\sum_{k=1}^{K}\sum_{i=1}^{n_k} \|d_i - c_k\|^2}{N-K}\right]} \tag{A2}$$

where d_i is the feature vector of data point i, n_k is the size of the k^{th} cluster, c_k is the feature vector of the centroid of the k^{th} cluster, c is the feature vector of the global centroid of the entire dataset, N is the total number of data points. The higher the score is the better separation.

Davies-Bouldin Index

$$R_{ij} = \frac{s_i + s_j}{d_{ij}} \tag{A3}$$

$$DBI = \frac{1}{k}\sum_{i=1}^{k} max_{i \neq j} R_{ij} \tag{A4}$$

where s_i is the average distance between each point of cluster i and the centroid of that cluster, d_{ij} is the distance between cluster centroids i and j. The score is between 0 and ∞, and the values closer to zero indicate a better separation.

Appendix C Classification metrics

For evaluating the predictions obtained to the FCN, we consider to compute the same metrics that the authors in [12] used for comparative purposes of this work. We compute through of the confusion matrix the equations shown follow:

Given a confusion matrix $\mathbf{M} \in \mathbb{R}^{C \times C}$ where C is the number of classes, the OA is computed with the equation A5.

$$OA = \frac{\sum_{i=1}^{C} \mathbf{M}_{ii}}{\sum_{i=1}^{C}\sum_{j=1}^{C} \mathbf{M}_{ij}} \tag{A5}$$

From $\mathbf{M}$ to a class-wise confusion matrix following the approach one versus all, the producers accuracy (PA) also known as precision is computed by

$$PA_c = \frac{TP_c}{TP_c + FP_c} \tag{A6}$$

where TP_c is the true positive and FP_c is the false positive of the class c.
Then, the average precision (AP) is computed as follows

$$AP = \frac{\sum_{c=1}^{C} PA_c}{C} \tag{A7}$$

The user's accuracy (UA_c) also known as recall is compute as follows

$$UA_c = \frac{TP_c}{TP_c + FN_c} \tag{A8}$$

where TP_c is the true positive and FN_c is the false negative of the class c.
With the equation A6 and A8 we can compute the F1-score per class ($F1_c$) as follows:

$$F1_c = 2\frac{PA_c \times UA_c}{PA_c + UA_c} \tag{A9}$$

and the weighted F1-score is computed by

$$F1 = \sum_{c=1}^{C} w_c \times F1_c \tag{A10}$$

where $w_c = \frac{N_c}{N}$ and N_c is the number of samples in class c and N denotes the total number of samples.

The formula for Cohen's kappa coefficient (κ) is the probability of agreement minus the probability of random agreement, divided by one minus the probability of random agreement.

$$\kappa = \frac{p_o - p_e}{1 - p_e} \tag{A11}$$

where p_o is is the relative observed agreement among raters, and p_e is the hypothetical probability of chance agreement.
The multiclass Matthew's correlation coefficient (MCC) is defined by

$$MCC = \frac{cp \times s - \sum_c^C p_c \times t_c}{\sqrt{(s^2 - \sum_c^C p_c^2) \times (s^2 - \sum_c^C t_c^2)}} \tag{A12}$$

where $t_c = \sum_i^C \mathbf{M}_{ic}$ represents the number of times that class c really happened., $p_c = \sum_i^C \mathbf{M}_{ci}$ denotes the number of times class c has been predicted , $cp = \sum_c^C \mathbf{M}_{cc}$ indicates the number of samples that have been correctly predicted and $s = \sum_i^C \sum_j^C \mathbf{M}_{ij}$ is the overall number of samples.

References

1. Vuolo, F.; Neuwirth, M.; Immitzer, M.; Atzberger, C.; Ng, W.T. How much does multi-temporal Sentinel-2 data improve crop type classification? *Int. J. Appl. Earth Obs.* **2018**, *72*, 122–130. https://doi.org/10.1016/j.jag.2018.06.007.
2. Pelletier, C.; Webb, G.; Petitjean, F. Temporal Convolutional Neural Network for the Classification of Satellite Image Time Series. *Remote Sensing* **2019**, *11*, 523. https://doi.org/10.3390/rs11050523.
3. Foerster, S.; Kaden, K.; Foerster, M.; Itzerott, S. Crop type mapping using spectral–temporal profiles and phenological information. *Comput. Electron. Agr.* **2012**, *89*, 30–40. https://doi.org/10.1016/j.compag.2012.07.015.
4. Chen, B.; Zheng, H.; Wang, L.; Hellwich, O.; Chen, C.; Yang, L.; Liu, T.; Luo, G.; Bao, A.; Chen, X. A joint learning Im-BiLSTM model for incomplete time-series Sentinel-2A data imputation and crop classification. *Int. J. Appl. Earth Obs.* **2022**, *108*, 102762. https://doi.org/10.1016/j.jag.2022.102762.
5. Tariq, A.; Yan, J.; Gagnon, A.S.; Riaz Khan, M.; Mumtaz, F. Mapping of cropland, cropping patterns and crop types by combining optical remote sensing images with decision tree classifier and random forest. *Geo-spatial Information Science* **2022**, *26*, 302–320. https://doi.org/10.1080/10095020.2022.2100287.
6. Gao, F.; Zhang, X. Mapping Crop Phenology in Near Real-Time Using Satellite Remote Sensing: Challenges and Opportunities. *Journal of Remote Sensing* **2021**, *2021*. https://doi.org/10.34133/2021/8379391.
7. Palchowdhuri, Y.; Valcarce-Diñeiro, R.; King, P.; Sanabria-Soto, M. Classification of multi-temporal spectral indices for crop type mapping: a case study in Coalville, UK. *The Journal of Agricultural Science* **2018**, *156*, 24–36. https://doi.org/10.1017/s0021859617000879.

8. Heupel, K.; Spengler, D.; Itzerott, S. A Progressive Crop-Type Classification Using Multitemporal Remote Sensing Data and Phenological Information. *PFG – Journal of Photogrammetry, Remote Sensing and Geoinformation Science* **2018**, *86*, 53–69. https://doi.org/10.1007/s41064-018-0050-7.
9. Li, Q.; Tian, J.; Tian, Q. Deep Learning Application for Crop Classification via Multi-Temporal Remote Sensing Images. *Agriculture-london.* **2023**, *13*, 906. https://doi.org/10.3390/agriculture13040906.
10. Dong, H.; Ma, W.; Wu, Y.; Zhang, J.; Jiao, L. Self-Supervised Representation Learning for Remote Sensing Image Change Detection Based on Temporal Prediction. *Remote Sensing* **2020**, *12*, 1868. https://doi.org/10.3390/rs12111868.
11. Paris, C.; Weikmann, G.; Bruzzone, L. Monitoring of agricultural areas by using Sentinel 2 image time series and deep learning techniques. In Proceedings of the Image and Signal Processing for Remote Sensing XXVI; Notarnicola, C.; Bovenga, F.; Bruzzone, L.; Bovolo, F.; Benediktsson, J.A.; Santi, E.; Pierdicca, N., Eds. SPIE, 2020. https://doi.org/10.1117/12.2574745.
12. Rußwurm, M.; Pelletier, C.; Zollner, M.; Lefèvre, S.; Körner, M. BREIZHCROPS: A TIME SERIES DATASET FOR CROP TYPE MAPPING. *The International Archives of the Photogrammetry, Remote Sensing and Spatial Information Sciences* **2020**, *XLIII-B2-2020*, 1545–1551. https://doi.org/10.5194/isprs-archives-xliii-b2-2020-1545-2020.
13. Nowakowski, A.; Mrziglod, J.; Spiller, D.; Bonifacio, R.; Ferrari, I.; Mathieu, P.P.; Garcia-Herranz, M.; Kim, D.H. Crop type mapping by using transfer learning. *International Journal of Applied Earth Observation and Geoinformation* **2021**, *98*, 102313. https://doi.org/10.1016/j.jag.2021.102313.
14. Gadiraju, K.K.; Vatsavai, R.R. Remote Sensing Based Crop Type Classification Via Deep Transfer Learning. *IEEE Journal of Selected Topics in Applied Earth Observations and Remote Sensing* **2023**, *16*, 4699–4712. https://doi.org/10.1109/jstars.2023.3270141.
15. Wu, B.; Zhang, M.; Zeng, H.; Tian, F.; Potgieter, A.B.; Qin, X.; Yan, N.; Chang, S.; Zhao, Y.; Dong, Q.; et al. Challenges and opportunities in remote sensing-based crop monitoring: a review. *National Science Review* **2022**, *10*. https://doi.org/10.1093/nsr/nwac290.
16. Yin, L.; You, N.; Zhang, G.; Huang, J.; Dong, J. Optimizing Feature Selection of Individual Crop Types for Improved Crop Mapping. *Remote Sensing* **2020**, *12*, 162. https://doi.org/10.3390/rs12010162.
17. Yi, Z.; Jia, L.; Chen, Q. Crop Classification Using Multi-Temporal Sentinel-2 Data in the Shiyang River Basin of China. *Remote Sensing* **2020**, *12*, 4052. https://doi.org/10.3390/rs12244052.
18. He, S.; Peng, P.; Chen, Y.; Wang, X. Multi-Crop Classification Using Feature Selection-Coupled Machine Learning Classifiers Based on Spectral, Textural and Environmental Features. *Remote Sensing* **2022**, *14*, 3153. https://doi.org/10.3390/rs14133153.
19. Dumeur, I.; Valero, S.; Inglada, J. Self-Supervised Spatio-Temporal Representation Learning of Satellite Image Time Series. *IEEE J. Sel. Topics Appl. Earth Observ. Remote Sens.* **2024**, *17*, 4350–4367. https://doi.org/10.1109/jstars.2024.3358066.
20. Wang, S.; Azzari, G.; Lobell, D.B. Crop type mapping without field-level labels: Random forest transfer and unsupervised clustering techniques. *Remote Sens. Environ.* **2019**, *222*, 303–317. https://doi.org/10.1016/j.rse.2018.12.026.
21. Maponya, M.G.; van Niekerk, A.; Mashimbye, Z.E. Pre-harvest classification of crop types using a Sentinel-2 time-series and machine learning. *Computers and Electronics in Agriculture* **2020**, *169*, 105164. https://doi.org/10.1016/j.compag.2019.105164.
22. Hu, Q.; Wu, W.; Song, Q.; Yu, Q.; Lu, M.; Yang, P.; Tang, H.; Long, Y. Extending the Pairwise Separability Index for Multicrop Identification Using Time-Series MODIS Images. *IEEE Trans. Geosci. Remote Sens.* **2016**, *54*, 6349–6361. https://doi.org/10.1109/tgrs.2016.2581210.
23. Roy, D.; Yan, L. Robust Landsat-based crop time series modelling. *Remote Sens. Environ.* **2020**, *238*, 110810. https://doi.org/10.1016/j.rse.2018.06.038.
24. Kussul, N.; Lavreniuk, M.; Skakun, S.; Shelestov, A. Deep Learning Classification of Land Cover and Crop Types Using Remote Sensing Data. *IEEE Geosci. Remote Sens. Lett.* **2017**, *14*, 778–782. https://doi.org/10.1109/lgrs.2017.2681128.
25. Inglada, J.; Vincent, A.; Arias, M.; Tardy, B.; Morin, D.; Rodes, I. Operational High Resolution Land Cover Map Production at the Country Scale Using Satellite Image Time Series. *Remote Sensing* **2017**, *9*, 95. https://doi.org/10.3390/rs9010095.
26. Cai, Y.; Guan, K.; Peng, J.; Wang, S.; Seifert, C.; Wardlow, B.; Li, Z. A high-performance and in-season classification system of field-level crop types using time-series Landsat data and a machine learning approach. *Remote Sens. Environ.* **2018**, *210*, 35–47. https://doi.org/10.1016/j.rse.2018.02.045.
27. Feng, S.; Zhao, J.; Liu, T.; Zhang, H.; Zhang, Z.; Guo, X. Crop Type Identification and Mapping Using Machine Learning Algorithms and Sentinel-2 Time Series Data. *IEEE J. Sel. Topics Appl. Earth Observ. Remote Sens.* **2019**, *12*, 3295–3306. https://doi.org/10.1109/jstars.2019.2922469.
28. Zhong, L.; Hu, L.; Zhou, H. Deep learning based multi-temporal crop classification. *Remote Sensing of Environment* **2019**, *221*, 430–443. https://doi.org/10.1016/j.rse.2018.11.032.
29. Prins, A.J.; Van Niekerk, A. Crop type mapping using LiDAR, Sentinel-2 and aerial imagery with machine learning algorithms. *Geo-spatial Information Science* **2020**, *24*, 215–227. https://doi.org/10.1080/10095020.2020.1782776.
30. Manish Lad, A.; Mani Bharathi, K.; Akash Saravanan, B.; Karthik, R. Factors affecting agriculture and estimation of crop yield using supervised learning algorithms. *Mater. Today:. Proc.* **2022**, *62*, 4629–4634. https://doi.org/10.1016/j.matpr.2022.03.080.
31. Agilandeeswari, L.; Prabukumar, M.; Radhesyam, V.; Phaneendra, K.L.N.B.; Farhan, A. Crop Classification for Agricultural Applications in Hyperspectral Remote Sensing Images. *Applied Sciences* **2022**, *12*, 1670. https://doi.org/10.3390/app12031670.
32. Tian, X.; Bai, Y.; Li, G.; Yang, X.; Huang, J.; Chen, Z. An Adaptive Feature Fusion Network with Superpixel Optimization for Crop Classification Using Sentinel-2 Imagery. *Remote Sensing* **2023**, *15*, 1990. https://doi.org/10.3390/rs15081990.

33. Rokach, L.; Maimon, O., Decision Trees. In *Data Mining and Knowledge Discovery Handbook*; Springer-Verlag; pp. 165–192. https://doi.org/10.1007/0-387-25465-x_9.
34. Chen, T.; Guestrin, C. XGBoost: A Scalable Tree Boosting System. In Proceedings of the Proceedings of the 22nd ACM SIGKDD International Conference on Knowledge Discovery and Data Mining. ACM, 2016, Vol. 11, *KDD '16*, pp. 785–794. https://doi.org/10.1145/2939672.2939785.
35. Breiman, L. *Mach. Learn.* **2001**, *45*, 5–32. https://doi.org/10.1023/a:1010933404324.
36. Cortes, C. Support-Vector Networks. *Mach. Learn.* **1995**.
37. Rosenblatt, F. The perceptron: A probabilistic model for information storage and organization in the brain. *Psychol. Rev.* **1958**, *65*, 386–408. https://doi.org/10.1037/h0042519.
38. Balestriero, R.; Ibrahim, M.; Sobal, V.; Morcos, A.; Shekhar, S.; Goldstein, T.; Bordes, F.; Bardes, A.; Mialon, G.; Tian, Y.; et al. A Cookbook of Self-Supervised Learning, 2023. https://doi.org/10.48550/ARXIV.2304.12210.
39. *Machine Learning for Data Science Handbook: Data Mining and Knowledge Discovery Handbook*; Springer International Publishing, 2023. https://doi.org/10.1007/978-3-031-24628-9.
40. Lopez Pinaya, W.H.; Vieira, S.; Garcia-Dias, R.; Mechelli, A., Autoencoders. In *Machine Learning*; Elsevier, 2020; pp. 193–208. https://doi.org/10.1016/b978-0-12-815739-8.00011-0.
41. Lopez-Fandino, J.; Garea, A.S.; Heras, D.B.; Arguello, F. Stacked Autoencoders for Multiclass Change Detection in Hyperspectral Images. In Proceedings of the IGARSS 2018 - 2018 IEEE International Geoscience and Remote Sensing Symposium. IEEE, 2018. https://doi.org/10.1109/igarss.2018.8518338.
42. Luppino, L.T.; Hansen, M.A.; Kampffmeyer, M.; Bianchi, F.M.; Moser, G.; Jenssen, R.; Anfinsen, S.N. Code-Aligned Autoencoders for Unsupervised Change Detection in Multimodal Remote Sensing Images. *IEEE Trans. Neural Netw. Learn. Syst.* **2024**, *35*, 60–72. https://doi.org/10.1109/tnnls.2022.3172183.
43. Kalinicheva, E.; Sublime, J.; Trocan, M., Change Detection in Satellite Images Using Reconstruction Errors of Joint Autoencoders. In *Artificial Neural Networks and Machine Learning – ICANN 2019: Image Processing*; Springer International Publishing, 2019; pp. 637–648. https://doi.org/10.1007/978-3-030-30508-6_50.
44. Lisaius, M.C.; Blake, A.; Keshav, S.; Atzberger, C. Using Barlow Twins to Create Representations From Cloud-Corrupted Remote Sensing Time Series. *IEEE J. Sel. Topics Appl. Earth Observ. Remote Sens.* **2024**, *17*, 13162–13168. https://doi.org/10.1109/jstars.2024.3426044.
45. Windrim, L.; Ramakrishnan, R.; Melkumyan, A.; Murphy, R.J.; Chlingaryan, A. Unsupervised Feature-Learning for Hyperspectral Data with Autoencoders. *Remote Sensing* **2019**, *11*, 864. https://doi.org/10.3390/rs11070864.
46. Bégué, A.; Arvor, D.; Bellon, B.; Betbeder, J.; de Abelleyra, D.; P. D. Ferraz, R.; Lebourgeois, V.; Lelong, C.; Simões, M.; R. Verón, S. Remote Sensing and Cropping Practices: A Review. *Remote Sensing* **2018**, *10*, 99. https://doi.org/10.3390/rs10010099.
47. Orynbaikyzy, A.; Gessner, U.; Conrad, C. Crop type classification using a combination of optical and radar remote sensing data: a review. *Int. J. Remote Sens.* **2019**, *40*, 6553–6595. https://doi.org/10.1080/01431161.2019.1569791.
48. Pierre Pott, L.; Jorge Carneiro Amado, T.; Augusto Schwalbert, R.; Mateus Corassa, G.; Antonio Ciampitti, I. Crop type classification in Southern Brazil: Integrating remote sensing, crop modeling and machine learning. *Comput. Electron. Agr.* **2022**, *201*, 107320. https://doi.org/10.1016/j.compag.2022.107320.
49. Moreno-Martínez, A.; Izquierdo-Verdiguier, E.; Maneta, M.P.; Camps-Valls, G.; Robinson, N.; Muñoz-Marí, J.; Sedano, F.; Clinton, N.; Running, S.W. Multispectral high resolution sensor fusion for smoothing and gap-filling in the cloud. *Remote Sens. Environ.* **2020**, *247*, 111901. https://doi.org/10.1016/j.rse.2020.111901.
50. Kandasamy, S.; Baret, F.; Verger, A.; Neveux, P.; Weiss, M. A comparison of methods for smoothing and gap filling time series of remote sensing observations – application to MODIS LAI products. *Biogeosciences* **2013**, *10*, 4055–4071. https://doi.org/10.5194/bg-10-4055-2013.
51. Tzelepi, M.; Nousi, P.; Passalis, N.; Tefas, A., Representation learning and retrieval. In *Deep Learning for Robot Perception and Cognition*; Elsevier, 2022; pp. 221–241. https://doi.org/10.1016/b978-0-32-385787-1.00015-4.
52. Reichstein, M.; Camps-Valls, G.; Stevens, B.; Jung, M.; Denzler, J.; Carvalhais, N.; Prabhat. Deep learning and process understanding for data-driven Earth system science. *Nature* **2019**, *566*, 195–204. https://doi.org/10.1038/s41586-019-0912-1.
53. Tschannen, M.; Djolonga, J.; Rubenstein, P.K.; Gelly, S.; Lucic, M. On Mutual Information Maximization for Representation Learning **2019**. [arXiv:cs.LG/1907.13625]. https://doi.org/10.48550/ARXIV.1907.13625.
54. Le-Khac, P.H.; Healy, G.; Smeaton, A.F. Contrastive Representation Learning: A Framework and Review. *IEEE Access* **2020**, *8*, 193907–193934. https://doi.org/10.1109/access.2020.3031549.
55. Aitchison, L.; Ganev, S. InfoNCE is variational inference in a recognition parameterised model, 2021. https://doi.org/10.48550/ARXIV.2107.02495.
56. Chen, T.; Kornblith, S.; Norouzi, M.; Hinton, G. A Simple Framework for Contrastive Learning of Visual Representations. In Proceedings of the Proceedings of the 37th International Conference on Machine Learning; III, H.D.; Singh, A., Eds. PMLR, 13–18 Jul 2020, Vol. 119, *Proceedings of Machine Learning Research*, pp. 1597–1607.
57. Bachman, P.; Hjelm, R.D.; Buchwalter, W. Learning Representations by Maximizing Mutual Information Across Views, 2019. https://doi.org/10.48550/ARXIV.1906.00910.
58. Dwibedi, D.; Aytar, Y.; Tompson, J.; Sermanet, P.; Zisserman, A. With a Little Help from My Friends: Nearest-Neighbor Contrastive Learning of Visual Representations, 2021. https://doi.org/10.48550/ARXIV.2104.14548.

59. Bardes, A.; Ponce, J.; LeCun, Y. VICReg: Variance-Invariance-Covariance Regularization for Self-Supervised Learning, 2021. https://doi.org/10.48550/ARXIV.2105.04906.
60. Zbontar, J.; Jing, L.; Misra, I.; LeCun, Y.; Deny, S. Barlow Twins: Self-Supervised Learning via Redundancy Reduction, 2021. https://doi.org/10.48550/ARXIV.2103.03230.
61. Coifman, R.R.; Lafon, S. Diffusion maps. *Appl. Comput. Harmon. A.* **2006**, *21*, 5–30. https://doi.org/10.1016/j.acha.2006.04.006.
62. Bank, D.; Koenigstein, N.; Giryes, R. Autoencoders, 2020. https://doi.org/10.48550/ARXIV.2003.05991.
63. Bank, D.; Koenigstein, N.; Giryes, R., Autoencoders. In *Machine Learning for Data Science Handbook*; Springer International Publishing, 2023; pp. 353–374. https://doi.org/10.1007/978-3-031-24628-9_16.
64. Zhang, L.; Qi, G.J.; Wang, L.; Luo, J. AET vs. AED: Unsupervised Representation Learning by Auto-Encoding Transformations rather than Data, 2019. https://doi.org/10.48550/ARXIV.1901.04596.
65. Baldi, P. Autoencoders, Unsupervised Learning, and Deep Architectures. In Proceedings of the Proceedings of ICML Workshop on Unsupervised and Transfer Learning; Guyon, I.; Dror, G.; Lemaire, V.; Taylor, G.; Silver, D., Eds., Bellevue, Washington, USA, 02 Jul 2012; Vol. 27, *Proceedings of Machine Learning Research*, pp. 37–49.
66. Dahlin, K.M.; Ponte, D.D.; Setlock, E.; Nagelkirk, R. Global patterns of drought deciduous phenology in semi-arid and savanna-type ecosystems. *Ecography* **2016**, *40*, 314–323. https://doi.org/10.1111/ecog.02443.
67. Foody, G.M. Status of land cover classification accuracy assessment. *Remote Sens. Environ.* **2002**, *80*, 185–201. https://doi.org/10.1016/s0034-4257(01)00295-4.